

Simulating quantum dynamics in two-dimensional lattices with tensor network influence functional belief propagation

Gunhee Park (박건희),¹ Johnnie Gray,² and Garnet Kin-Lic Chan²

¹*Division of Engineering and Applied Science, California Institute of Technology, Pasadena, California 91125, USA*

²*Division of Chemistry and Chemical Engineering,
California Institute of Technology, Pasadena, California 91125, USA*

Describing nonequilibrium quantum dynamics remains a significant computational challenge due to the growth of spatial entanglement. The tensor network influence functional (TN-IF) approach mitigates this problem for computing the time evolution of local observables by encoding the subsystem's influence functional path integral as a matrix product state (MPS), thereby shifting the resource governing computational cost from spatial entanglement to temporal entanglement. We extend the applicability of the TN-IF method to two-dimensional lattices by demonstrating its construction on tree lattices and proposing a belief propagation (BP) algorithm for the TN-IF, termed influence functional BP (IF-BP), to simulate local observable dynamics on arbitrary graphs. Even though the BP algorithm introduces uncontrolled approximation errors on arbitrary graphs, it provides an accurate description for locally tree-like lattices. Numerical simulations of the kicked Ising model on a heavy-hex lattice, motivated by a recent quantum experiment, highlight the effectiveness of the IF-BP method, which demonstrates superior performance in capturing long-time dynamics where traditional tensor network state-based methods struggle. Our results further reveal that the temporal entanglement entropy (TEE) only grows logarithmically with time for this model, resulting in a polynomial computational cost for the whole method. We further construct a cluster expansion of IF-BP to introduce loop correlations beyond the BP approximation, providing a systematic correction to the IF-BP estimate. We demonstrate the power of the cluster expansion of the IF-BP in simulating the quantum quench dynamics of the 2D transverse field Ising model, obtaining numerical results that improve on the state-of-the-art.

I. INTRODUCTION

Describing nonequilibrium quantum dynamics is a formidable challenge, even in one-dimensional systems, due to the exponential growth of the Hilbert space with system size. For equilibrium properties, the area-law scaling of spatial entanglement allows for the efficient representation of ground states using tensor network (TN) states [1]. In nonequilibrium settings, however, the situation is markedly different. In generic thermalizing systems, the entanglement entropy typically grows linearly in time, even when starting from an initially weakly entangled state [2, 3]. This growth results in an exponential increase in computational cost for simulating quantum dynamics with TN states.

To circumvent the exponential cost, numerous methods have been proposed to simulate the dynamics of local observables without requiring a full representation of the quantum state [4–12]. Among these, we focus on the tensor network influence functional (TN-IF) approach [13–28]. The influence functional (IF) concept originates from the open quantum system description of quantum dynamics [29], where the system is divided into a subsystem and a bath. The subsystem contains the degrees of freedom associated with the observable of interest, while the IF captures the time-nonlocal influence of the bath through a path integral over the subsystem's trajectories after tracing out the bath. Recent studies have demonstrated that the IF can often be efficiently

represented as a compact, low-rank matrix product state (MPS) along the time direction. Most prior work has focused on IFs derived from Gaussian baths [15–17, 23–28], one-dimensional (1D) interacting baths [13, 14, 17–21], or separable interacting baths [22].

This paper aims to extend the TN-IF method's applicability to two-dimensional (2D) lattice models. To address the complexity inherent to 2D systems, we begin by constructing the TN-IF for dynamics on tree lattices. The absence of loops in tree lattices ensures that the structure of the IF closely resembles that found in 1D systems. Building on this tree construction, we introduce a belief propagation (BP) algorithm adapted to the IF, which we refer to as influence functional BP (IF-BP), for simulating dynamics on arbitrary graphs. The BP algorithm, originally developed for probabilistic graphical models [30–32], has recently been explored in the context of general tensor network contractions [33–39]. While the BP algorithm introduces an uncontrolled approximation, it often achieves reasonable accuracy on locally tree-like lattices with large loops.

The efficacy of the proposed approach is illustrated through numerical simulations of the kicked Ising model on a heavy-hex lattice, inspired by recent quantum experiments with IBM's superconducting qubit processor [40]. The large-loop structure of the heavy-hex lattice facilitates the application of TN states and TN operators with BP approximations. These methods have shown high accuracy in classical simulations, successfully capturing the

dynamics up to the experimental timescale of 20 Trotter steps [38, 41–43]. Nonetheless, while BP-approximated TN states perform well at short times, their applicability is ultimately constrained by the growth of spatial entanglement, which can result in exponential computational costs for longer-time simulations.

Numerical results using the IF-BP show enhanced classical simulation performance already at 20 Trotter steps for specific parameter regimes. For longer-time dynamics, the IF-BP successfully captures the magnetization of an infinite-temperature state in agreement with predictions from Floquet thermalization [44–46]. In contrast, the time-propagated TN states with finite bond dimension exhibit an unphysical increase in magnetization. The computational advantage of the IF-BP is attributed to the slow growth of the temporal entanglement entropy [18, 19], which here increases *logarithmically* with time. The resulting logarithmic scaling suggests that the MPS representation of the IF requires only a polynomial computational cost.

We further extend the TN-IF framework beyond the BP approximation to account for loop effects in general loopy graphs, such as square lattices, by employing a cluster expansion. This approach allows us to systematically correct the uncontrolled approximations inherent in the BP limit, improving accuracy for graphs with significant loop contributions. To demonstrate the effectiveness of this extension, we analyze the quench dynamics of the transverse field Ising model on a square lattice - a case where the BP solution alone fails to provide accurate results due to the pronounced influence of loops. Comparisons with several methods, including TN state propagation, sparse Pauli dynamics [47], and neural quantum Galerkin methods [48], demonstrate the state-of-the-art accuracy of our approach.

II. TENSOR NETWORK INFLUENCE FUNCTIONALS ON TREE LATTICES

A. Dynamics on one-dimensional lattices

In this section, we formulate tensor network influence functionals on tree lattices. Before considering the dynamics on tree lattices, we first review tensor network influence functionals on 1D lattices [13, 17–19], which are the simplest type of tree lattice. We consider a time evolution of a 1D system starting from a matrix product state (MPS) $|\psi_0\rangle$. We assume time evolution is described by a unitary matrix product operator (MPO) [49], denoted as \hat{U} . A time-evolved wavefunction after m applications of the MPO can be written as $|\psi(m)\rangle = \hat{U}_m \cdots \hat{U}_2 \hat{U}_1 |\psi_0\rangle$. Our goal is to compute an expectation value of a local single-site observable \hat{O} , $\langle \hat{O}(m) \rangle = \langle \psi(m) | \hat{O} | \psi(m) \rangle$. A tensor network (TN) diagram representing this expectation value is illustrated in Fig. 1a, and has a two-dimensional (2D) TN structure.

Computing the expectation value from the TN diagram

requires contracting the 2D space-time TN. The accuracy and computational cost of 2D TN contraction depend on the TN contraction path and approximation scheme. One standard way of contracting a 2D TN is to approximate the boundary of the 2D TN with an MPS [50–53]. The standard contraction path represents $|\psi(m)\rangle$ as a fixed bond-dimension MPS and contracts the time evolution along the time direction.

Ref. [13] proposed a new strategy for contracting the space-time TN along the spatial direction, referring to this as a transverse contraction. One significant observation is that the accuracy of the transverse contraction improves after folding the TN in half and grouping the ket and bra parts ($|\psi(m)\rangle$ and $\langle \psi(m)|$, respectively) as in Fig. 1b. The folded TN is contracted transversely towards the column with \hat{O} ($\mathcal{T}_{\hat{O}}$ in Fig. 1b), and the intermediate boundary tensors are approximated with MPS with a fixed bond dimension. After contracting all the tensors on the left and right sides of $\mathcal{T}_{\hat{O}}$, we obtain two MPSs, denoted by \mathcal{I} and pink tensors in Fig. 1c. The expectation value of the local observable \hat{O} is computed by an overlap of the two \mathcal{I} with the MPO $\mathcal{T}_{\hat{O}}$ in the middle.

In recent years, the above folding strategy has been re-interpreted in the language of tensor network influence functionals (TN-IF) [17–19]. The folded TN in Fig. 1b can be expressed as $\text{Tr}[\hat{O} \mathcal{U}_m \cdots \mathcal{U}_2 \mathcal{U}_1 \hat{\rho}_0]$ where $\hat{\rho}_0 = |\psi_0\rangle\langle\psi_0|$ and the superoperator \mathcal{U} is defined by $\mathcal{U} \bullet = \hat{U} \bullet \hat{U}^\dagger$. The sites outside of \hat{O} are viewed as a bath, and the transverse contraction effectively traces out the bath, only leaving its influence on the dynamics of the subsystem. This effect of a bath on a system's dynamics was originally formulated by Feynman and Vernon [29] in terms of an influence functional (IF) path integral over the system density operator degrees of freedom for baths consisting of harmonic oscillators linearly coupled to the system. The contracted MPS \mathcal{I} defines an influence functional [54] for arbitrary many-body quantum baths and couplings. We describe this object as an influence functional MPS (IF-MPS).

The IF-MPS approach provides a controlled way to approximate the local expectation value by increasing the bond dimension of the IF-MPS. The IF-MPS \mathcal{I} can be obtained in a finite system by propagating (contracting) the tensor network in the spatial direction starting from a spatial boundary. In a translationally invariant infinite system, we can further formulate an equation to find the leading eigenvector of the transfer matrix \mathcal{T} in Fig. 1b and 1d, which then serves as an effective spatial boundary.

The contraction of the IF-MPS along the spatial direction reduces to a 1D TN contraction of grouped tensors, where each grouped tensor corresponds to a column of tensors associated with a single spatial site (Fig. 1d). Since arbitrary 1D TN can be contracted exactly, and the resulting effective tensor contraction can be efficiently carried out using the boundary MPS procedure, this provides a practical computational algorithm. Building on this approach, we next extend the formulation of TN-IF

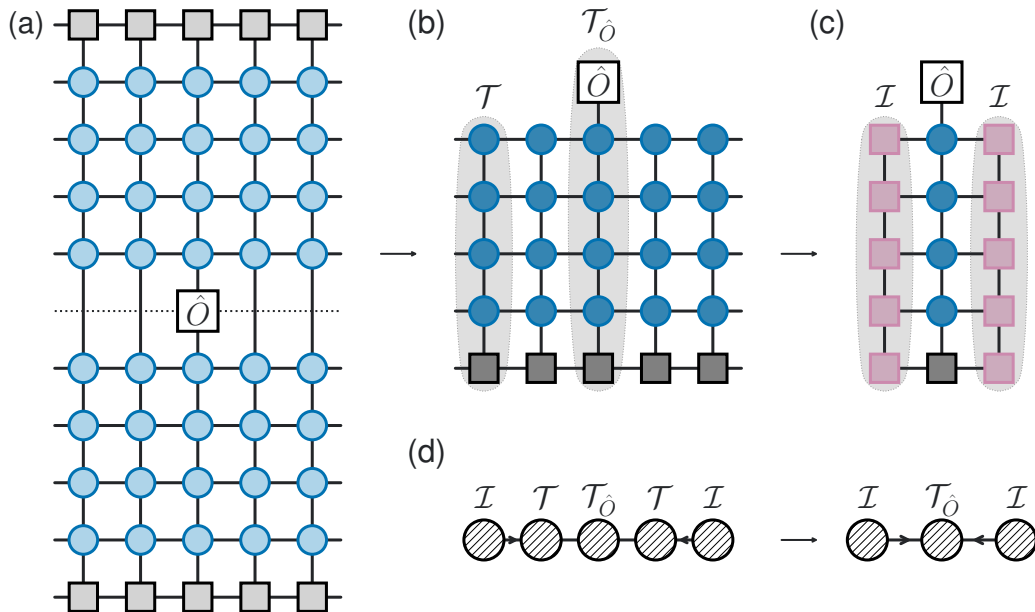


FIG. 1. Tensor network diagram illustrating dynamics on a one-dimensional lattice. (a) Tensor network diagram for a local observable expectation value $\langle \hat{O}(m) \rangle = \langle \psi(m) | \hat{O} | \psi(m) \rangle$ where $m = 4$ in this figure. The initial state $|\psi_0\rangle$ is given by a matrix product state (MPS) (light gray squares), and time evolution is carried out by a matrix product operator (MPO) (light blue circles). (b) A folded tensor network (folded TN), where the folding occurs along the dashed line in (a). The darker shaded tensors denote doubly grouped tensors from (a). Tensors from the same spatial site are grouped together as \mathcal{T} or $\mathcal{T}_{\hat{O}}$, shown with the light gray shading. (c) We contract the folded TN in (b) along the transverse direction around the site with \hat{O} . The boundary tensors are approximated by an MPS with a fixed bond dimension during the transverse contraction. The final MPS \mathcal{I} (pink squares) is called an influence functional MPS (IF-MPS). (d) One-dimensional structure of the IF-MPS propagation after grouping tensors by spatial sites.

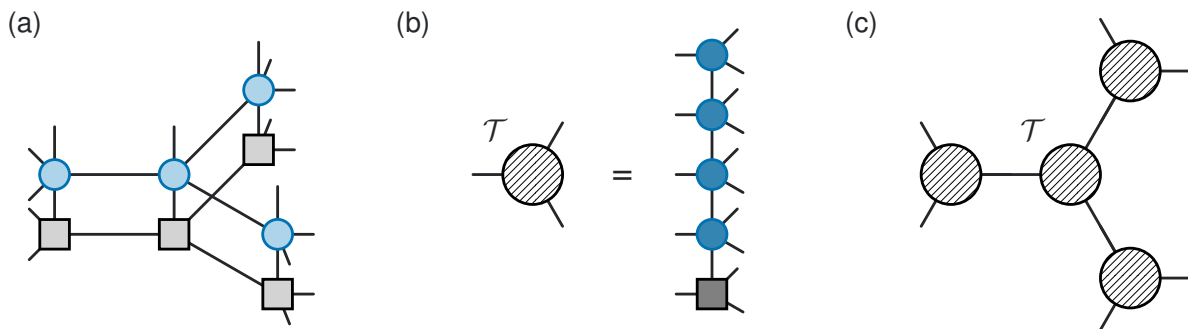


FIG. 2. Tensor network diagram illustrating dynamics on a tree lattice. (a) The initial state is a tree tensor network state, and its time evolution is carried out by a tree tensor network operator. (b) After folding the TN $\langle \hat{O}(m) \rangle$, we group tensors in the same spatial site as \mathcal{T} . (c) A grouped tensor \mathcal{T} within a tree tensor network.

to tree lattices.

B. Dynamics on tree lattices

Now we consider dynamics on tree lattices. We assume that the initial state is a tree tensor network state, and a time evolution step is carried out by a tensor network operator with the same connectivity as the tree lattice,

i.e., a tree tensor network operator, \hat{U} in Fig. 2a. The folded TN for $\langle \hat{O}(m) \rangle = \langle \psi(m) | \hat{O} | \psi(m) \rangle$ is constructed analogously to in 1D lattices. By grouping the column of tensors on the same site as \mathcal{T} (Fig. 2b), we have a tree tensor network composed of the grouped tensors \mathcal{T} (Fig. 2c).

Like in the 1D case, this tree tensor network has an efficient contraction path. Therefore, we can use the boundary contraction algorithm in conjunction with this path

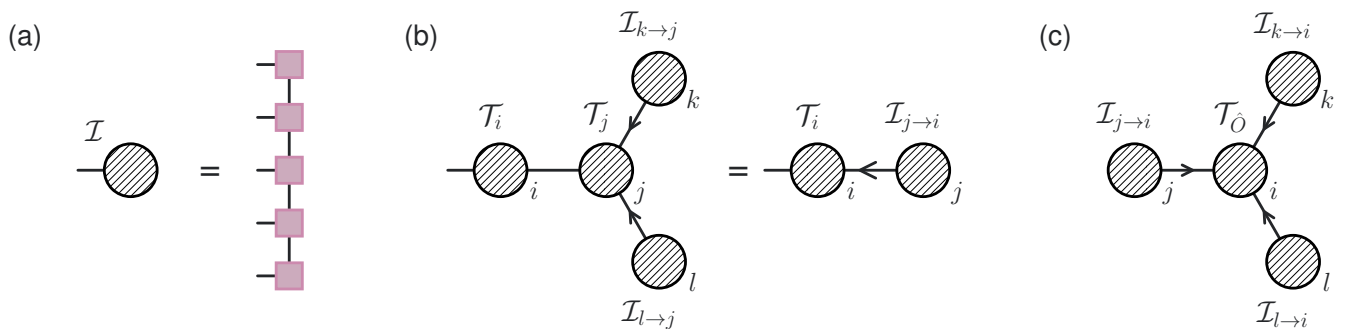


FIG. 3. (a) IF-MPS \mathcal{I} for the tree subgraph at each bond. (b) TN contraction of two IF-MPSs $\mathcal{I}_{k \rightarrow j}$ and $\mathcal{I}_{l \rightarrow j}$ from sites k and l with the tensor \mathcal{T}_j at site j . This creates a new IF-MPS $\mathcal{I}_{j \rightarrow i}$ directed from site j to site i . (c) Final TN diagram after the IF-MPSs reach the site of interest with the operator \hat{O} . The desired expectation value is computed from the contraction of this TN.

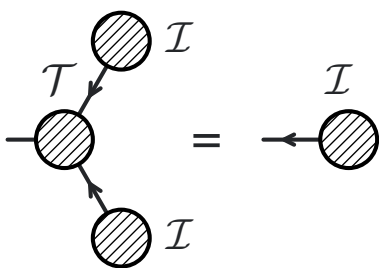


FIG. 4. Self-consistent equation for IF-MPS in the $z = 3$ Bethe lattice assuming rotational invariance.

to contract the network, similar to the strategy used in the 1D lattice dynamics discussed above. In the previous section, we also related the boundary MPS contraction of a folded TN to the IF-MPS. Here, we extend the concept of IF-MPS to tree lattices.

At each bond extending from a site in the tree lattice, the subgraph from the bond also forms a tree disconnected from the tree subgraphs formed by the other bonds. For finite tree lattices, each subgraph is terminated by end-sites that only have a single bond; for such an end-site, the corresponding tensor \mathcal{I} has an MPS structure along the time axis (Fig. 3a), which defines an initial IF-MPS for the end-site. The main difference between 1D and tree lattice dynamics is that as we contract inwards from the end-sites, multiple IF-MPSs are combined at the same site. For example, in Fig. 3b, two sites k and l are connected around site j with tensor \mathcal{T}_j , with IF-MPS $\mathcal{I}_{k \rightarrow j}$ and $\mathcal{I}_{l \rightarrow j}$. Here, we draw arrows on the bonds and subscripts to indicate the propagation direction more clearly. After contracting \mathcal{T}_j , $\mathcal{I}_{k \rightarrow j}$, and $\mathcal{I}_{l \rightarrow j}$, the new IF-MPS $\mathcal{I}_{j \rightarrow i}$ is created directed towards the site i . The bond dimension of $\mathcal{I}_{j \rightarrow i}$ can be truncated to a smaller finite bond dimension using MPS compression. In a later section, we will discuss a more efficient numerical scheme to directly construct $\mathcal{I}_{j \rightarrow i}$ with a given bond dimension. We iterate this propagation until we reach

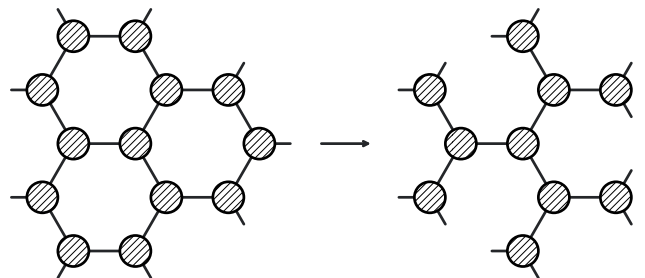


FIG. 5. (Left) Tensor network diagram on an infinite hexagonal lattice. (Right) Within the belief propagation (BP) approximation, the fixed point BP equation is equivalent to that on the $z = 3$ Bethe lattice.

the site of interest with \hat{O} , and the desired expectation value is computed from the contraction of the final TN as in Fig. 3c.

It is straightforward to extend the above procedure for finite tree lattices to infinite tree lattices with the same coordination number, known as Bethe lattices [55]. Given the IF-MPS \mathcal{I} for one tree subgraph, the subgraph itself is composed of the tensor \mathcal{T} and $z - 1$ IF-MPS \mathcal{I} where z is the coordination number of the Bethe lattice. Fig. 4 illustrates the case when $z = 3$. From the above condition, we see that the IF-MPS satisfies a non-linear self-consistent equation.

III. BELIEF PROPAGATION WITH INFLUENCE FUNCTIONALS

This section introduces a belief propagation (BP) algorithm for IF-MPS, which we call influence functional belief propagation (IF-BP). IF-BP describes a numerical scheme to find the (self-consistent) IF-MPS \mathcal{I} and to evaluate local expectation values using the IF-MPS. This algorithm applies to both tree and locally tree-like lattices. When the underlying graph is a tree, the ac-

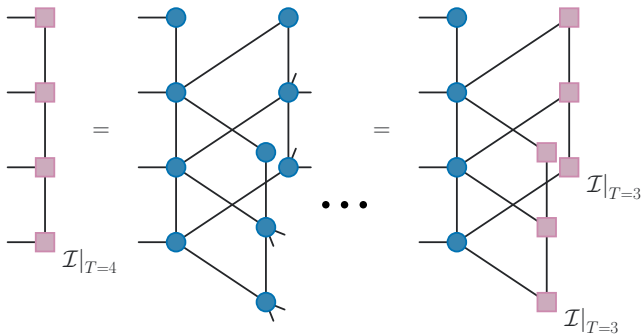


FIG. 6. The IF-MPS from the Bethe lattice has a light cone structure. The light cone IF-MPS follows an iterative structure, where the IF-MPS at $T = 4$, $\mathcal{I}|_{T=4}$, can be constructed from two IF-MPSs at $T = 3$, $\mathcal{I}|_{T=3}$.

curacy of expectation values computed using IF-BP is controlled only by the bond dimension of the IF-MPS. When the graph is not exactly a tree, the IF-BP expectation values are not exact anymore, even in the infinite bond dimension limit. Nonetheless, the BP algorithm often provides good heuristic estimates when the graph is locally tree-like [32].

We start with the folded TN, where we group tensors by their sites as in Fig. 2c, but within a general lattice with loops. IF-MPSs are initialized at each bond for both directions. For example, two IF-MPSs $\mathcal{I}_{i \rightarrow j}^{(0)}$ and $\mathcal{I}_{j \rightarrow i}^{(0)}$ are initialized at the bond between sites i and j . The IF-BP involves iterative local propagation of the IF-MPS, similar to the propagation in Fig. 3b,

$$\mathcal{I}_{j \rightarrow i}^{(t+1)} = \mathcal{T}_j \cdot \bigotimes_{k \in \partial j \setminus i} \mathcal{I}_{k \rightarrow j}^{(t)}, \quad (1)$$

where $\partial j \setminus i$ denotes a set of neighbor sites of j excluding site i and \cdot denotes a tensor contraction. We repeat the propagation until Eq. 1 reaches a fixed point; it forms a local self-consistent BP equation [31, 32],

$$\mathcal{I}_{j \rightarrow i} = \mathcal{T}_j \cdot \bigotimes_{k \in \partial j \setminus i} \mathcal{I}_{k \rightarrow j}. \quad (2)$$

The BP equation in the tree graph reduces to the exact propagation described in the previous section.

We remark that the BP equation introduced in this section resembles the BP equation for probabilistic graphical models [31, 32] or tensor networks [33–36]. The BP equation in the above references is based on a ‘message-passing’ algorithm where the message plays the role of the IF-MPS in this work. Unlike the standard message-passing algorithm, the main difference here is that the IF-MPS is approximated as a low-rank MPS with a fixed bond dimension during propagation [56].

The BP approximation becomes clearer when considering the dynamics of an infinite translation-invariant lattice, such as a hexagonal lattice in Fig. 5. In this limit, if the initialized IF-MPSs in each bond are invariant with

respect to translations and rotations, the fixed point BP equation for the hexagonal lattice becomes identical to the self-consistent equation for the $z = 3$ Bethe lattice in Fig. 4. Therefore, a BP approximated dynamics on the infinite hexagonal lattice yields a $z = 3$ Bethe lattice dynamics (Fig. 5).

Using the Bethe lattice reduction, the fixed point IF-MPS on the infinite lattice can be directly obtained from a light cone on the Bethe lattice for the unitary dynamics. As illustrated in Fig. 6, the light cone IF-MPS follows an iterative structure, where the IF-MPS at $T = 4$, $\mathcal{I}|_{T=4}$, can be constructed from two IF-MPSs at $T = 3$, $\mathcal{I}|_{T=3}$,

$$\mathcal{I}_{j \rightarrow i}|_{T=4} = \mathcal{T}_j|_{T=4} \cdot \bigotimes_{k \in \partial j \setminus i} \mathcal{I}_{k \rightarrow j}|_{T=3}. \quad (3)$$

This light cone construction for the IF-MPS offers additional numerical advantages, even in 1D systems [20, 57], as the intermediate IF-MPS exhibits lower entanglement entropy.

Either with the IF-BP equation in Eq. 1 or with the light cone propagation in Eq. 3, the bond dimension of the IF-MPS increases during the propagation, so bond dimension truncation during the propagation is necessary. An iterative singular value decomposition (SVD) is a standard way to truncate MPS, but it becomes expensive at large z . If the bond dimension of $\mathcal{I}_{k \rightarrow j}^{(t)}$ and \mathcal{T}_j is D and d , respectively, the bond dimension of $\mathcal{I}_{j \rightarrow i}^{(t+1)}$ without truncation is dD^{z-1} for coordination number z . The computational cost of the SVD becomes $\mathcal{O}(D^{3(z-1)})$. Instead, we construct $\mathcal{I}_{j \rightarrow i}^{(t+1)}$ with a lower bond dimension directly from a variational optimization by minimizing the distance,

$$d\left(\mathcal{I}_{j \rightarrow i}^{(t+1)}\right) = \left\| \mathcal{I}_{j \rightarrow i}^{(t+1)} - \mathcal{T}_j \cdot \bigotimes_k \mathcal{I}_{k \rightarrow j}^{(t)} \right\|^2. \quad (4)$$

The optimal solution can be found by an alternating least squares (ALS) optimization. This performs the least squares minimization for one tensor in $\mathcal{I}_{j \rightarrow i}^{(t+1)}$ at a time with the other tensors fixed and sweeps across the tensors in $\mathcal{I}_{j \rightarrow i}^{(t+1)}$ iteratively. This method has previously been utilized for MPO-MPS multiplication [50, 52, 53, 58, 59].

The leading computational cost of the ALS method depends on the computation of an overlap tensor network contraction,

$$\mathcal{I}_{j \rightarrow i}^{(t+1)*} \cdot \mathcal{T}_j \cdot \bigotimes_k \mathcal{I}_{k \rightarrow j}^{(t)}. \quad (5)$$

The computational complexity of this tensor network contraction is $\mathcal{O}(D^{z+1})$, lower than that of the SVD truncation for $z > 2$.

IV. PERFECT DEPHASER POINT

Belief propagation provides a numerical scheme to obtain the MPS approximation of IF. Even though an an-

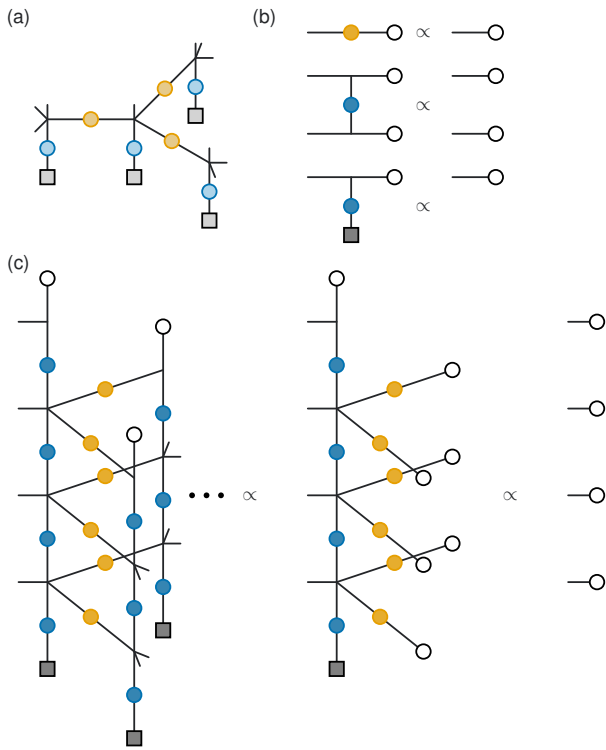


FIG. 7. Tensor network diagram for the dynamics of the kicked Ising model at its perfect dephaser (PD) point. (a) Time evolution is given by a local X rotation (light blue circles) and nearest neighbor ZZ interaction (light orange circles). (b) A dual-unitary property of the self-dual points. White circles indicate a local trace operation. (c) Tensor network diagram of the IF from the light cone construction of the folded TN. The IF is reduced to a product form with the local trace operations recursively, where the IF satisfies the PD property.

analytical expression for the IF cannot be obtained in general, Ref. [18] discusses a class of dynamics on 1D lattices where analytical expressions can be obtained, called the perfect dephaser (PD) point, where the IF has a product form at each time that effectively dephases the system. This section provides examples of the PD point IF on tree lattices from dynamics within the family of kicked Ising models.

We start from a kicked Ising model described by the following Trotterized time evolution,

$$\hat{U} = \prod_{\langle j,k \rangle} e^{i\theta_J \hat{Z}_j \hat{Z}_k / 2} \prod_j e^{-i\theta_h \hat{X}_j / 2}, \quad (6)$$

where $\langle j, k \rangle$ denotes the nearest neighbor pair on tree lattices. We will consider a simple product state as an initial state, $|\psi_0\rangle = \otimes_i |0_i\rangle$, and application of \hat{U} for m Trotter steps, $|\psi(m)\rangle = \hat{U}^m |\psi_0\rangle$. Fig. 7a shows a graphical tensor network diagram of this time evolution. In the 1D kicked Ising model, the IF satisfies the PD property at $|\theta_J| = \pi/2$ and $|\theta_h| = \pi/2$, which coincides with the self-dual points of the kicked Ising model [60, 61].

Each gate at the self-dual points satisfies a dual-unitary property [61], where its diagrammatic representation is illustrated in Fig. 7b. White circles in the figure indicate a local trace operation. We also note that the gates at the given parameters are Clifford.

We show that these properties hold for Bethe lattices. We prove the PD property from the light cone construction of the folded TN to build the IF in Fig. 7c. The consequent IF has a product form of local trace operations. The proof is based on the recursive structure of the tree. The light-cone IF with time n ($n = 4$ in Fig. 7c) has subtrees with time $n - 1$. For the recursion, assuming the local trace operation form of IF at time $n - 1$, the local trace form of IF at time n is derived from the dual-unitary property (Fig. 7c). A broader class of models also leads to a PD form of the IF if the constituting circuits satisfy the dual-unitary property or a generalization, such as in tri-unitary quantum circuits [62].

In the case of the kicked Ising model on loopy lattices, the local self-consistent BP equation reduces the problem to the Bethe lattice, resulting in the exact product form of the IF-MPS, which completely dephases the local density operator. The local reduced density operator undergoing the PD point kicked Ising dynamics also becomes an infinite-temperature thermal ensemble $\hat{\rho} \propto |0\rangle\langle 0| + |1\rangle\langle 1|$, thus agreeing with the analysis from the BP approximation.

V. DYNAMICS ON HEAVY-HEX LATTICE

A. Kicked Ising model on heavy-hex lattice

We now study the dynamics of the kicked Ising model on an infinite heavy-hex lattice, where the qubits are placed on both the vertices and edges of a hexagonal lattice (Fig. 8). We denote each site as a v site or e site for the vertex and edge qubits, respectively. The time evolution operator for the kicked Ising model is given by Eq. 6. A recent experimental study of the dynamics on this lattice using a quantum processor [40] has led to the development of various numerical methods for the classical simulation of the dynamics [38, 41–43, 63–66].

In this section, we compare our results with those obtained by time-evolving projected entangled-pair states (PEPS) or operators (PEPO) combined with belief propagation [35, 36, 38, 41]. In this context, belief propagation is employed to determine the gauge of the tensor network states or operators at a fixed time, or to compute expectation values after the time evolution is complete. Previous studies have shown that the BP approximation accurately described local observables and that spatial loop correlations were negligible in the heavy-hex lattice. Nonetheless, the required bond dimensions to achieve converged results were large in a few parameter regimes, and even larger bond dimensions are expected for deeper circuit simulations due to entanglement growth. These characteristics make the system a suitable testbed for the

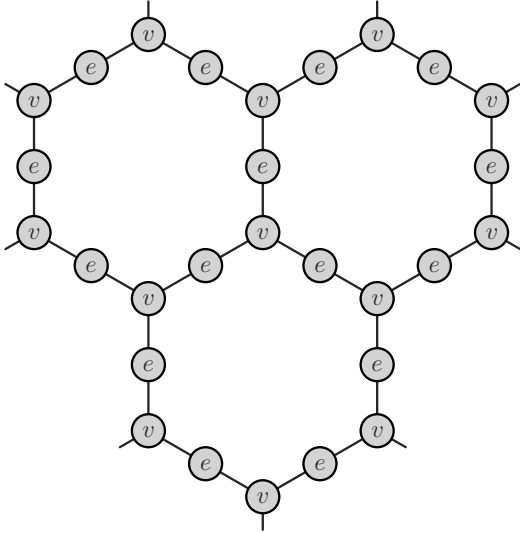


FIG. 8. Geometry of a heavy-hex lattice. Qubits are placed at the vertices (v) and edges (e) of a hexagonal lattice.

IF-BP method.

B. Numerical results

1. Numerical details

Away from the perfect dephaser point, the fixed-point IF-MPS is obtained through iterative propagation using Eq. 1. In this section, we assume translational and rotational invariance across the v and e sites in Fig. 8. The ZZ -type interaction terms in the folded TN (orange circles in Fig. 7b) act on pairs of sites, resulting in a structure that differs from that shown in Fig. 2b and 2c. We decompose the two-site operators by SVD, splitting them into single-site contributions. The square roots of the singular values, $s^{1/2}$, are symmetrically absorbed into the adjacent sites. This decomposition yields a TN with the same geometry as in Fig. 2b and 2c [67].

The IF-MPS is now characterized by two MPSs, $\mathcal{I}_{v \rightarrow e}^{(t)}$ and $\mathcal{I}_{e \rightarrow v}^{(t)}$. The update rule from Eq. 1 becomes,

$$\mathcal{I}_{v \rightarrow e}^{(t+1)} = \mathcal{T}_v \cdot \left(\mathcal{I}_{e_1 \rightarrow v}^{(t)} \otimes \mathcal{I}_{e_2 \rightarrow v}^{(t)} \right), \quad (7)$$

where \mathcal{T}_v denotes the grouped tensor network at site v and the sites e_1 and e_2 are two different incoming edge sites. Even though we distinguish e_1 and e_2 , the IF-MPSs $\mathcal{I}_{e_1 \rightarrow v}^{(t)}$ and $\mathcal{I}_{e_2 \rightarrow v}^{(t)}$ are actually the same IF-MPS $\mathcal{I}_{e \rightarrow v}^{(t)}$, due to the assumption of rotational symmetry. We can apply the same update rule for $\mathcal{I}_{e \rightarrow v}^{(t+1)}$ from $\mathcal{I}_{v \rightarrow e}^{(t)}$, but we observed that the following update rule with $\mathcal{I}_{v \rightarrow e}^{(t+1)}$ has a better convergence,

$$\mathcal{I}_{e \rightarrow v}^{(t+1)} = \mathcal{T}_e \cdot \mathcal{I}_{v \rightarrow e}^{(t+1)}. \quad (8)$$

This modified update rule can be understood from the iterative IF-MPS propagation in the corresponding Bethe lattice with alternating coordination numbers, $z = 2$ and $z = 3$.

Another important numerical detail is the initial guess for the IF-MPS, $\mathcal{I}_{e \rightarrow v}^{(0)}$. Ref. [19, 57] reported that the IF-MPS propagation could encounter a high (temporal) entanglement barrier depending on the initial guess, even if the entanglement of the final fixed-point IF-MPS is low. For a moderate bond dimension, we choose the initial guess IF-MPS to be the fixed point IF-MPS of the 1D lattice kicked Ising model with the same Hamiltonian parameters [68]. For larger bond dimensions, we use the fixed-point IF-MPS of the lower bond dimension as an initial guess. These initial guesses converge to the fixed-point IF-MPS in a few iterations.

For numerical stability, we normalize the IF-MPS with norm 1, $\|\mathcal{I}^{(t)}\|^2 = 1$ after each propagation step. We iterate the update until we satisfy the convergence criterion, $1 - \left| \mathcal{I}_{v \rightarrow e}^{(t)*} \cdot \mathcal{I}_{v \rightarrow e}^{(t+1)} \right| < \epsilon$ with $\epsilon = 10^{-6}$. When we compute the expectation value of local observables $\langle \hat{O} \rangle$, we normalize the expectation value so that its total trace is 1, i.e., $\langle \hat{\mathbb{I}} \rangle = 1$, where $\hat{\mathbb{I}}$ is an identity operator.

2. Shallow depth circuit results

We fix $\theta_J = \pi/2$ and vary θ_h between zero and $\pi/2$ with $\theta_h = k\pi/32$, $k \in [0, 1, 2, \dots, 16]$ following the original experiment. First, we compute the magnetization on the v -sites, $\langle \hat{Z}_v(m) \rangle$, at Trotter steps $m = 9$ and $m = 20$, as shown in Fig. 9. The $m = 9$ results are compared with exact benchmarks after light cone cancellation [38, 40] (Fig. 9a). At this Trotter step $m = 9$, the maximum error is less than 5×10^{-3} using a very small bond dimension for the IF-MPS, $D = 8$, and smaller than 6×10^{-4} for bond dimension $D = 32$.

We now discuss the $m = 20$ results, for which no exact benchmark is available. We compare our result with those from infinite PEPS (iPEPS) calculations with the BP approximation and the results from Ref. [38], which employed the ‘MIX TN’ method. In that method, half of the time evolution is carried out using a PEPS, and the other half using a PEPO. Ref. [38] reported that the MIX TN method yields the most accurate results and the fastest convergence with bond dimension among the methods considered. While their results are based on simulations of a finite 127-qubit system, we assume the finite-size effects to be small [41, 64]. Fig. 9b compares the results from the IF-BP with $D = 320$, iPEPS with $D = 512$, and the best results from the MIX TN in [38]. Across most values of θ_h , all three methods show good agreement, except for a slight deviation of the iPEPS results for $\theta_h = 9, 10, 11\pi/32$.

In Fig. 10, we analyze the convergence behavior of the three methods with respect to bond dimension at $\theta_h = 7, 8, 9, 10\pi/32$. At $\theta_h = 7\pi/32$, all three methods

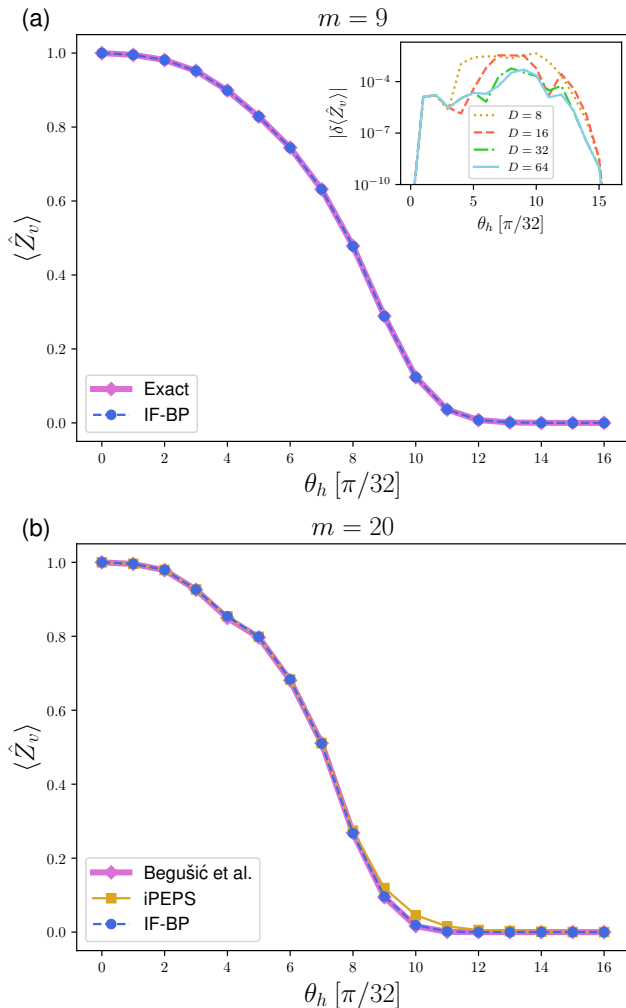


FIG. 9. Magnetization on a v site $\langle \hat{Z}_v \rangle$ at Trotter step (a) $m = 9$ and (b) $m = 20$ while varying θ_h . (a) At $m = 9$, the IF-BP results (blue circles) are compared to the exact benchmark from [38] (thick pink line). The inset shows the errors with respect to the exact benchmark at different bond dimensions. (b) At $m = 20$, the IF-BP results are compared to the MIX TN method results from [38] (thick pink line) and iPEPS results (yellow squares).

converge without the need for bond dimension extrapolation. However, for larger values of θ_h , the iPEPS results are not as fully converged at $D = 512$ as those obtained from IF-BP and MIX TN, which accounts for the discrepancy observed in Fig. 9. Notably, at $\theta_h = 9\pi/32$ and $10\pi/32$, the IF-BP result exhibits faster convergence than both iPEPS and MIX TN methods.

We analyze the above convergence behavior by estimating the relevant entanglement entropy (EE) from the IF-BP and iPEPS methods in Fig. 11. For the IF-BP method, we compute the EE of IF-MPS, known as the temporal entanglement entropy (TEE) [18, 19]. We have two TEEs because there are two different IF-MPSs, $\mathcal{I}_{e \rightarrow v}$ and $\mathcal{I}_{v \rightarrow e}$. For the iPEPS method, we compute the EE

at each bond of the iPEPS [41]. The EE of the iPEPS increases at larger θ_h , whereas the TEE of IF-MPS decreases for $\theta_h > 8\pi/32$. The IF-MPS with $\theta_h = \pi/2$ corresponds to an IF-MPS at the perfect dephaser point where the TEE is zero, which explains the above TEE trend and supports the fast convergence of the IF-BP method at $\theta_h = 9\pi/32$ and $\theta_h = 10\pi/32$. It is worth mentioning that a larger EE does not necessarily indicate lower accuracy, especially when comparing the EE of iPEPS and the TEE of IF-MPS. For example, at $\theta_h = 7\pi/32$, the EE of iPEPS is lower than the TEE of IF-MPS, but the convergence behaviors of the two methods are similar [69].

3. Longer time dynamics

In this section, we present numerical results for longer-time dynamics. The EE of the wavefunction generally grows linearly with time, and TN wavefunction methods, including the iPEPS method, require exponentially growing bond dimensions. Fig. 12 shows the time-dependence of the magnetization $\langle \hat{Z}_v \rangle$ and EE at $\theta_h = 10\pi/32$ from the IF-BP and iPEPS methods with various bond dimensions up to Trotter step $m = 40$. The magnetization from the IF-BP method already produces a converged result by a smaller bond dimension of $D = 128$. The magnetization reaches a near-zero value corresponding to an infinite-temperature thermal ensemble from the Floquet thermalization [44–46]. In contrast, the iPEPS simulation shows an unphysical magnetization increase in the long-time limit. The unphysical behavior can be traced back to the plateau in the EE at long times ($m \gtrsim 20$) due to the limited bond dimension, which does not reproduce the expected linear growth of EE with time. The TEE of the IF-BP in Fig. 12, on the other hand, is fully converged with respect to the bond dimension and does not grow linearly but grows logarithmically with time.

In Fig. 13, we illustrate that the logarithmic increase of the TEE holds in various parameter regimes by varying θ_h at fixed $\theta_J = \pi/2$ (Fig. 13a) and by varying $\theta_J = \theta_h = \theta$ (Fig. 13b). In this calculation, we use bond dimension $D = 128$, based on the converged behavior of the IF-BP TEE in Fig. 12, and show the TEE of the IF-MPS $\mathcal{I}_{e \rightarrow v}$.

4. Kicked Ising model with additional longitudinal field

Previous studies in [18, 70–72] have related the logarithmic increase of TEE to the integrability. In particular, the kicked Ising model with a transverse field in a 1D lattice is exactly solvable after a Jordan-Wigner transformation to a free fermion model and shows an area-law or logarithmic behavior of TEE [70, 72]. Unlike the 1D model, the Jordan-Wigner transformation does not map the kicked Ising model to a free-fermionic model on the heavy-hex lattice (or the Bethe lattice). Nonetheless, the observation in the previous section suggests that the TEE

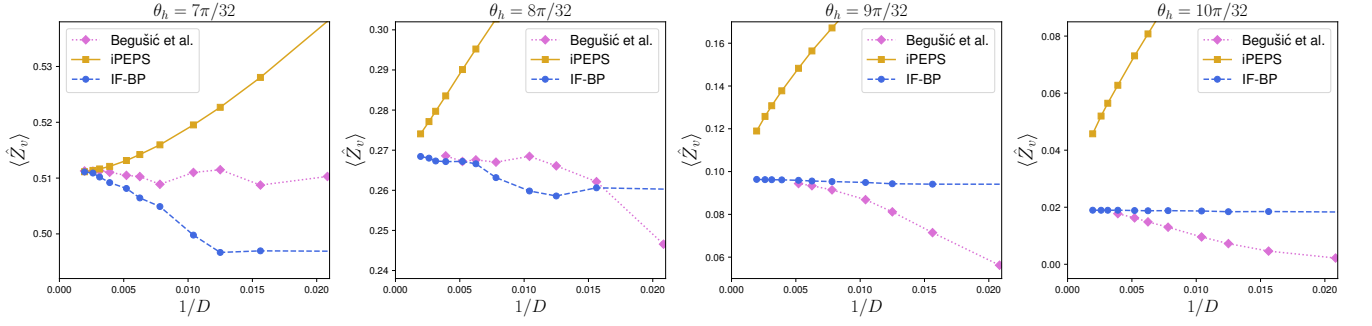


FIG. 10. The convergence of magnetization $\langle \hat{Z}_v \rangle$ at $m = 20$ Trotter steps with respect to bond dimension at $\theta_h = 7, 8, 9, 10\pi/32$ with the MIX TN (pink dotted), iPEPS (yellow solid), and IF-BP (blue dashed) methods.

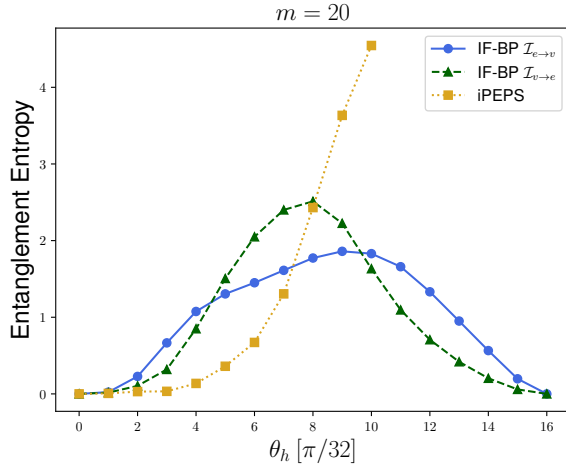


FIG. 11. Entanglement entropy from the IF-BP and iPEPS methods varying θ_h at Trotter step $m = 20$. The IF-BP curves show the temporal entanglement entropy of two different IF-MPS, $\mathcal{I}_{e \rightarrow v}$ (blue circles) and $\mathcal{I}_{v \rightarrow e}$ (green diamonds). The iPEPS curve (yellow square) refers to the entanglement entropy computed at each bond.

still grows logarithmically in this model up to the Trotter step $m = 40$.

The integrability of the 1D kicked Ising model is broken by adding a longitudinal field. We consider the following Trotterized time evolution with a longitudinal field:

$$\hat{U} = \prod_{\langle j,k \rangle} e^{i\theta_J \hat{Z}_j \hat{Z}_k / 2} \prod_j e^{-i\theta_h \hat{X}_j / 2} e^{-i\theta_l \hat{Z}_j / 2}, \quad (9)$$

where θ_l controls the longitudinal field strength. Ref. [18, 70] report a regime where the TEE grows linearly with time in the kicked Ising model with a longitudinal field. Fig. 14 shows the TEE behavior varying θ_l at (a) $\theta_J = \pi/2$, $\theta_h = 10\pi/32$, and (b) $\theta_J = 10\pi/32$, $\theta_h = 10\pi/32$ for kicked Ising dynamics on the heavy-hex lattice. The TEE behavior in the heavy-hex lattice shows a logarithmic or sublogarithmic increase with time, even after adding the longitudinal field. For $\theta_J = \pi/2$, $\theta_h = 10\pi/32$, the TEE even decreases at larger θ_l . This behavior is qualitatively

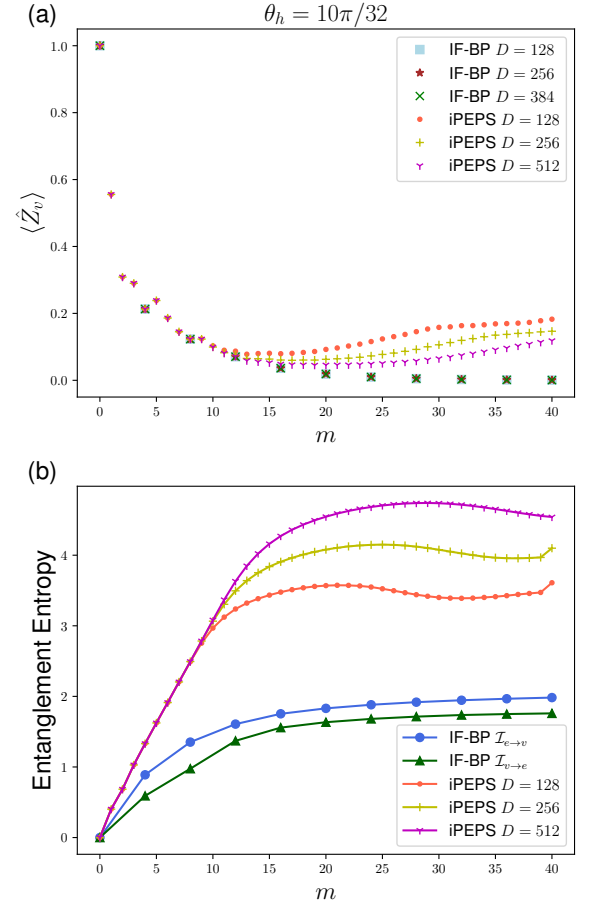


FIG. 12. Time-dependence of (a) magnetization $\langle \hat{Z}_v \rangle$ and (b) entanglement entropy at $\theta_h = 10\pi/32$ from the IF-BP and iPEPS methods with various bond dimensions. The entanglement entropy from the IF-BP method in (b) is a converged result with respect to the bond dimension.

different from the TEE scaling in the 1D kicked Ising model.

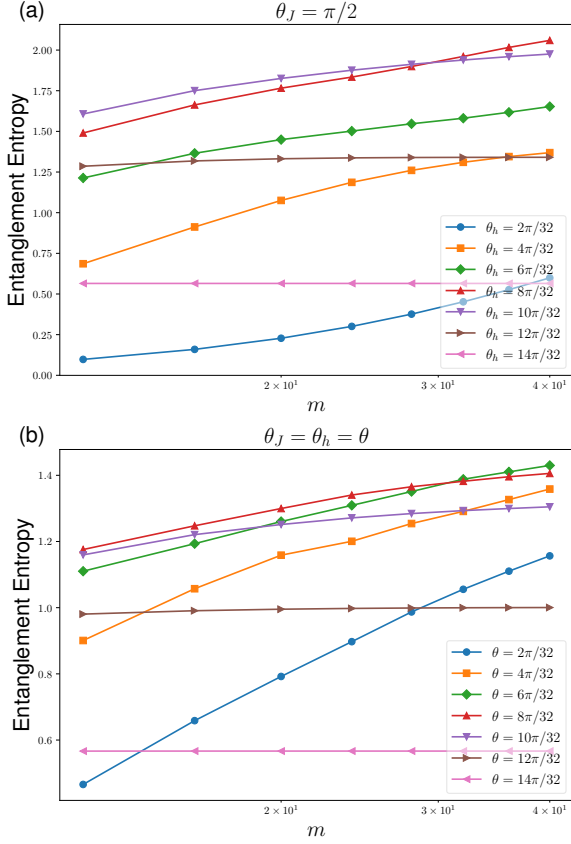


FIG. 13. Logarithmic increase of temporal entanglement entropy in the IF-BP method for the IF-MPS $\mathcal{I}_{e \rightarrow v}$ when (a) varying θ_h with fixed θ_J and (b) varying $\theta_J = \theta_h = \theta$. The m axis uses a logarithmic scale.

VI. CLUSTER EXPANSION OF THE TENSOR NETWORK INFLUENCE FUNCTIONAL

A. Method

The BP solution provides an accurate result when the underlying graph is locally tree-like. Nevertheless, in a general loopy graph, such as a graph over a square lattice, the BP solution gives an uncontrolled approximation, because it ignores loop correlations. Numerous efforts have been made to introduce loop corrections in both classical [30, 73–81] and quantum [82] systems.

We now describe a method to include the loop effects of quantum dynamics that are neglected in the IF-BP solution using a cluster expansion, similar to the loop series expansion presented in [82]. We first consider a single cluster region around the local observable of interest and use the BP solution to define its boundary. Fig. 15a illustrates a cluster of maximum loop width $W = 2$ surrounded by its BP environment. This cluster idea has previously been used to compute local observable expectation values with PEPS wavefunction [83, 84].

The cluster expansion combines expectation values

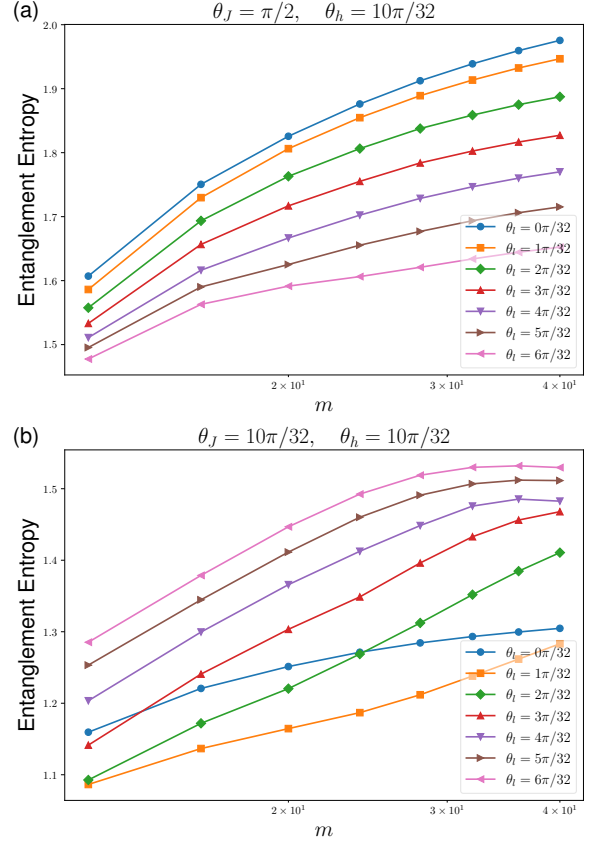


FIG. 14. Temporal entanglement entropy scaling after adding the longitudinal field at (a) $\theta_J = \pi/2, \theta_h = 10\pi/32$, and (b) $\theta_J = 10\pi/32, \theta_h = 10\pi/32$. The strength of the longitudinal field is controlled by θ_t . The m axis uses a logarithmic scale.

from multiple overlapping regions to determine an improved local observable expectation value. For example, in Fig. 15b, the region with width $W = 2$ can be obtained by patching together four smaller regions with loop width $W = 1$. Different regions share overlapping regions around the local observable. The counting number of the overlapping regions is evaluated based on the inclusion-exclusion principle [85], including its sign to avoid double-counting. As drawn in Fig. 15c, the cluster expansion up to $W = 1$ includes 4-site, 2-site, and 1-site regions with counting numbers 4, -4, and 1, respectively. The factor of 4 reflects the rotational invariance of the dynamics. Using the equations satisfied by the BP solution, further reductions can be made to locally tree-like regions, such as reducing the 2-site region to a 1-site region, resulting in the counting number -3 for the 1-site region.

In general, by patching together regions with maximum loop width W , one can cover a region with maximum loop width $2W$, after which a counting number $c(r)$ is assigned to each region r based on the inclusion-exclusion principle. This counting scheme has been exploited in many different numerical schemes, such as gen-

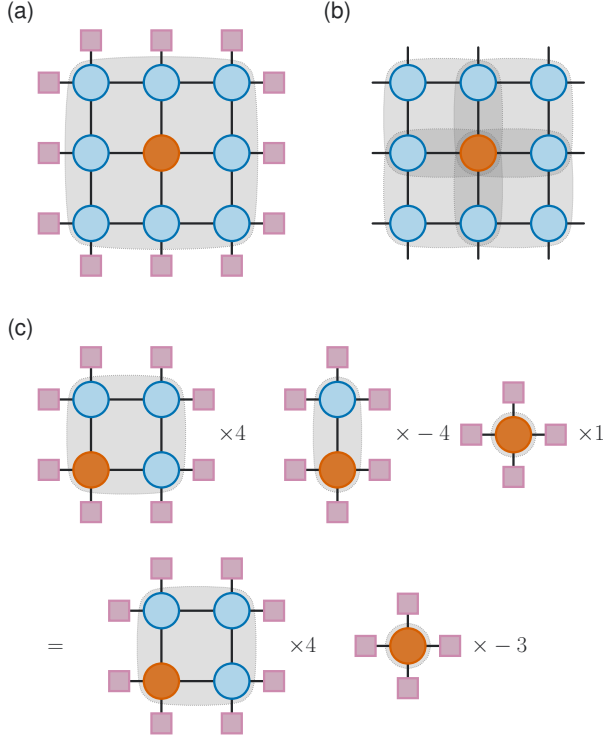


FIG. 15. (a) A finite cluster around the local observable located in the center (red) with a maximum loop width $W = 2$ surrounded by BP environments (pink). (b) The region with width $W = 2$ can be patched together from four smaller clusters with loop width $W = 1$. The cluster expansion uses the counting number of overlapping regions based on the inclusion-exclusion principle. (c) Cluster expansion up to $W = 1$ includes 4-site, 2-site, and 1-site clusters with counting numbers 4, -4, and 1, respectively. The 2-site cluster with a tree geometry can be further reduced to the 1-site cluster by using the BP equations.

eralized BP [30] and the numerical linked-cluster expansion [85]. The local observable expectation can then be computed with the counting number $c(r)$, using $\langle \hat{O} \rangle_r$ to denote the expectation value from each region r , either by a weighted arithmetic mean,

$$\langle \hat{O} \rangle \approx \sum_r c(r) \times \langle \hat{O} \rangle_r, \quad (10)$$

or by a weighted geometric mean,

$$\langle \hat{O} \rangle \approx \prod_r \langle \hat{O} \rangle_r^{c(r)}, \quad (11)$$

In practice, we find that the two yield numerically similar values, with differences between the two much smaller than the remaining error due to the finite loop width W . Henceforth, unless otherwise specified, we use the expansion with the weighted arithmetic mean in Eq. 10.

After assigning the regions, we need to compute $\langle \hat{O} \rangle_r$ by contracting the tensor network within this region. We

note that the region is defined as a subgraph on the 2D lattice above. However, there is also the time direction perpendicular to the lattice, where we express the BP environment using the IF-MPS. Using exact contraction, the contraction cost scales exponentially with the number of sites in the region. Instead, we employ approximate contraction by compressing bonds between nearest neighbor sites during contractions over the time direction. We utilize the ‘simple update’ algorithm [86, 87] for this compression, which features a bond-local gauge structure akin to that of BP compression [33, 36, 38], but without implementing self-consistency over the graph. This type of simple update compression can be less accurate than BP compression due to a less self-consistent local gauge. However, we have found the loss of accuracy to be negligible here, while using this simple update reduces the computational cost by a significant factor. We propagate the tensor network with simple update compression from the initial state to the local observable and use boundary MPS contraction [50–53] for the final 2D tensor network. Propagation in this direction allows us to reuse tensor network intermediates for multiple regions with the same shape, but where the local observable is located in a different part of the region.

B. Numerical results

We test the performance of the cluster expansion of the TN-IF by simulating the quench dynamics of the transverse field Ising model (TFIM),

$$\hat{H} = -J \sum_{\langle j,k \rangle} \hat{Z}_j \hat{Z}_k - h \sum_j \hat{X}_j, \quad (12)$$

on the 2D square lattice. Various numerical methods, such as iPEPS [88–90], neural quantum methods [48, 91], and sparse Pauli dynamics (SPD) [47], have been employed to simulate the quench dynamics of the 2D TFIM. We consider quench dynamics from an initial state that is the ground state for $h \rightarrow \infty$, i.e., $|\psi_0\rangle = \bigotimes_j |+\rangle_j$ where $|+\rangle = (|0\rangle + |1\rangle)/\sqrt{2}$, and use a quenched Hamiltonian with $h = h_c$ and $h = 2h_c$, where $h_c = 3.04438$ corresponds to the quantum critical point [92], and $J = 1$. For the time evolution operator \hat{U} we use the second-order Trotter decomposition,

$$\hat{U} = \prod_j e^{i\Delta t \hat{X}_j/2} \prod_{\langle j,k \rangle} e^{i\Delta t \hat{Z}_j \hat{Z}_k} \prod_j e^{i\Delta t \hat{X}_j/2}. \quad (13)$$

Fig. 16 shows the time-dependence of the local observable expectation value $\langle \hat{X}(t) \rangle$ up to time $t = 1.0$ from the IF-BP and its cluster expansion compared to data from the SPD [47], iPEPS [90], and time-dependent Neural Quantum Galerkin (t-NQG) [48, 93] methods. The cluster IF-BP data shown in Fig. 16 corresponds to the largest cluster size used in our calculations; for the final four time points, results from a cluster size with one loop

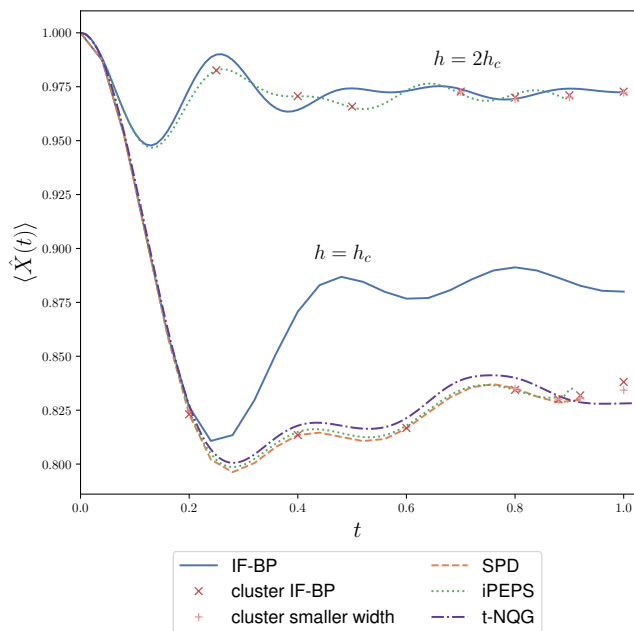


FIG. 16. Time-dependence of the local observable expectation value $\langle \hat{X}(t) \rangle$ of 2D TFIM after the quench from the X-polarized state to $h = h_c$ and $h = 2h_c$, where $h_c = 3.04438$ is a critical point. We compute these dynamics using IF-BP and its cluster expansion and compare to reference data from sparse Pauli dynamics (SPD) [47], iPEPS [90], and time-dependent Neural Quantum Galerkin (t-NQG) [48, 93] methods. For the final four time points, results from a cluster size with one loop width smaller are included to illustrate the convergence behavior.

width smaller are also included to illustrate the convergence behavior. A more detailed analysis of the convergence with respect to cluster size is presented in a later paragraph. We aim to compare our result to the SPD data for $h = h_c$ and the iPEPS data for $h = 2h_c$. Therefore, we set the timestep $\Delta t = 0.04$ and $\Delta t = 0.01$ for the quenches with $h = h_c$ and $h = 2h_c$, respectively, corresponding to the timesteps used in the SPD and iPEPS simulations. As an estimate of the corresponding timestep error, Ref. [47] reported that the Trotter timestep error at $h = h_c$ is less than 0.003 in the observable, which agrees well with the scale of deviation between SPD and iPEPS. The t-NQG method exhibits negligible error from timestep discretization in the numerical integration.

We note that the SPD and t-NQG methods are implemented on finite systems. Specifically, SPD is run on an 11×11 lattice with open boundary conditions, while t-NQG uses an 8×8 lattice with periodic boundary conditions. In Fig. 16 at $h = h_c$, some differences are observed among the reference data obtained from SPD, iPEPS, and t-NQG. To investigate the origin of these differences, we additionally performed SPD simulations on an 8×8 lattice with periodic boundary conditions, as shown in Fig. 17 up to $t = 0.6$. The SPD method contains a controllable threshold parameter δ that enables us to verify

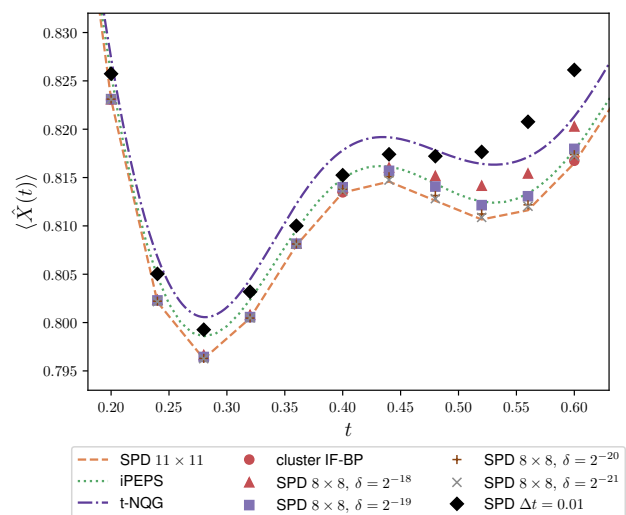


FIG. 17. Finite-size analysis of the SPD method applied to an 8×8 lattice with periodic boundary conditions, matching the setup of the t-NQG method. Convergence of the SPD method is controlled by the threshold parameter δ . We find that the finite size effect of the SPD method is negligible.

numerical convergence. By decreasing δ from 2^{-18} to 2^{-21} , we observe that the results on the 8×8 lattice converge to those from the 11×11 system, thereby ruling out finite-size effects as the source of discrepancy. Fig. 17 also includes SPD data with $\Delta t = 0.01$ and $\delta = 2^{-19}$, taken from Ref. [47]. We note that the SPD method generally requires a smaller δ to achieve comparable accuracy. Despite this, the SPD data shows good agreement with the iPEPS results up to $t = 0.4$, confirming that the visible discrepancies arise from the timestep error. Given the timestep error estimate of 0.003 from Ref. [47] and the comparison to iPEPS data with $\Delta t = 0.01$, most of the remaining deviation of the t-NQG data likely originates from the limited variational expressivity of the particular neural quantum parametrization.

We first find the IF-BP estimate of the observable, constructing the IF-MPS through light cone propagation, as described in Eq. 3. The IF-BP estimate demonstrates rapid convergence with respect to the bond dimension of the IF-MPS, achieving full convergence at $D = 16$ for $t = 1.0$ for both $h = h_c$ and $h = 2h_c$. For $h = 2h_c$, the IF-BP estimate of the expectation value provides an accurate solution, with errors of less than 0.01 compared to that from the iPEPS simulation. In contrast, the expectation values from the IF-BP technique at $h = h_c$ accurately capture the dynamics in the short-time limit ($t < 0.2$) but exhibit noticeable deviations for $t > 0.2$.

Next, we incorporate loop effects through the cluster expansion. In Fig. 18, we show cluster IF-BP results with various maximum loop widths W . For $h = 2h_c$, the cluster expansion converges rapidly with respect to W , achieving convergence to within 0.002 at $W = 4$ and showing good agreement with the iPEPS data. However,

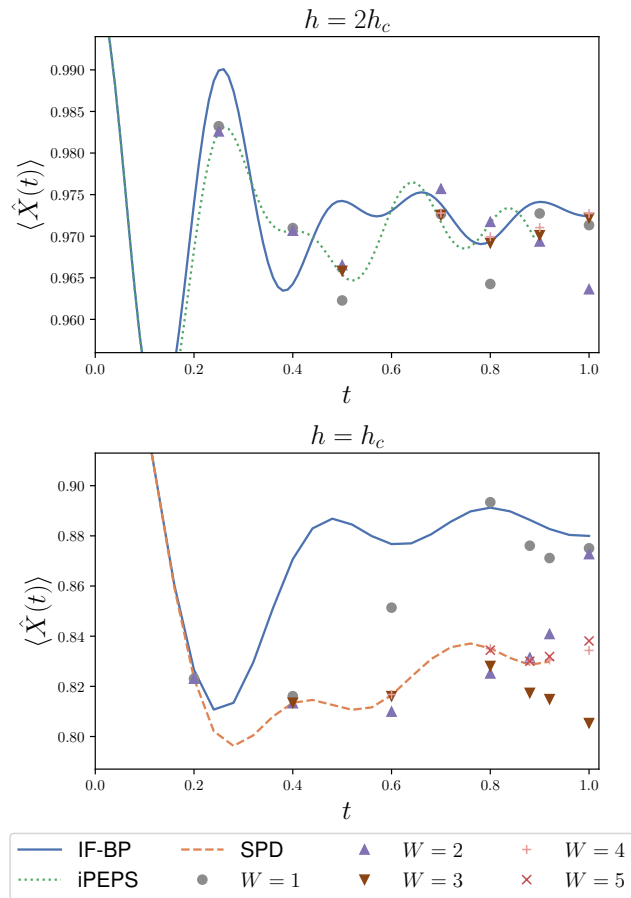


FIG. 18. Convergence of $\langle \hat{X}(t) \rangle$ using a cluster expansion of IF-BP by varying maximum loop widths W at $h = 2h_c$ (top) and $h = h_c$ (bottom).

for $h = h_c$, an accurate description requires larger W for the longer-time dynamics. For instance, the results with $W = 1$ and $W = 2$ remain accurate up to $t = 0.4$ but deviate beyond $t = 0.6$. Similarly, the results with $W = 3$ begin to deviate at $t = 0.8$. Nevertheless, results with $W = 4$ and $W = 5$ show good convergence to the reference SPD data up to $t = 0.92$, with errors of less than 0.002.

Another factor determining the computational cost of the cluster expansion is the intermediate bond dimension D_{SU} used in the SU compression and the boundary MPS contraction of the clusters. In our calculations, the boundary MPS bond dimension was set equal to D_{SU} , which provided sufficient accuracy. The required D_{SU} increases with t to maintain accuracy in the tensor network contraction. Specifically, the required D_{SU} to converge to the SPD reference data at $h = h_c$ is 24, 40, 56, and 64 for $t = 0.4, 0.6, 0.8$, and $0.8 < t < 1.0$, respectively. While $D_{\text{SU}} = 72$ was used for $t = 1.0$, this did not yield fully converged results for large W , resulting in an estimated uncertainty of 0.005 in the observable. Consequently, the visible difference between $W = 4$ and $W = 5$ at $t = 1.0$

in Fig. 18 arises not only from loop effects but also from insufficient convergence in D_{SU} .

VII. CONCLUSIONS

In this work, we introduced the belief propagation (BP) algorithm based on tensor network influence functionals to simulate the dynamics of local observables in quantum lattice systems beyond one dimension. The method is numerically exact on tree lattices in the limit of large bond dimensions and remains accurate on locally tree-like lattices with large loops. Our numerical results validate the effectiveness of IF-BP by reproducing the kicked Ising dynamics quantum experiments on the heavy-hex lattice. Moreover, for longer-time dynamics, the IF-BP approach outperforms traditional tensor network state-based methods, as it leverages the slow, logarithmic growth of temporal entanglement entropy to maintain computational efficiency.

To address the limitations of BP on graphs with loops, we developed a cluster expansion of the tensor network influence functionals. By enlarging clusters around the subsystem and combining expectation values from overlapping regions, the method systematically incorporates loop-induced correlations and provides controlled improvements in accuracy beyond the BP approximation. We demonstrated the effectiveness of this approach by simulating the quench dynamics of the transverse field Ising model on a 2D square lattice, where loop effects are prominent. The cluster expansion produced results that are competitive with, and in some cases improve upon, existing state-of-the-art methods, underscoring its potential as a practical tool for simulating nonequilibrium dynamics in 2D quantum systems. In addition to advancing classical simulation techniques, such numerical methods also provide a valuable tool for benchmarking quantum devices [40, 94, 95].

VIII. ACKNOWLEDGEMENTS

We thank Jacek Dziarmaga, Tomislav Begušić, and Alessandro Sinibaldi for sharing the iPEPS [90], SPD [47], and t-NQG [48, 93] data, respectively, presented in Fig. 16. The authors thank Tomislav Begušić, Giuseppe Carleo, Filippo Vicentini, and Alessandro Sinibaldi for helpful discussions. This material is based upon work supported by the U.S. Department of Energy, Office of Science, Office of Advanced Scientific Computing Research and Office of Basic Energy Sciences, Scientific Discovery through Advanced Computing (SciDAC) program under Award Number DE-SC0022088. The `quimb` library [96] has been used in the numerical experiments. Computations presented here were conducted in the Resnick High Performance Computing Center, a facility supported by Resnick Sustainability Institute at the California Institute of Technology. G.P. acknowledges

support from the Eddleman Quantum Graduate Fellowship at Caltech.

-
- [1] J. I. Cirac, D. Pérez-García, N. Schuch, and F. Verstraete, Matrix product states and projected entangled pair states: Concepts, symmetries, theorems, *Rev. Mod. Phys.* **93**, 045003 (2021).
- [2] P. Calabrese and J. Cardy, Evolution of entanglement entropy in one-dimensional systems, *Journal of Statistical Mechanics: Theory and Experiment* **2005**, P04010 (2005).
- [3] H. Kim and D. A. Huse, Ballistic spreading of entanglement in a diffusive nonintegrable system, *Phys. Rev. Lett.* **111**, 127205 (2013).
- [4] C. D. White, M. Zaletel, R. S. K. Mong, and G. Refael, Quantum dynamics of thermalizing systems, *Phys. Rev. B* **97**, 035127 (2018).
- [5] D. Tamascelli, A. Smirne, S. F. Huelga, and M. B. Plenio, Nonperturbative treatment of non-markovian dynamics of open quantum systems, *Phys. Rev. Lett.* **120**, 030402 (2018).
- [6] J. Surace, M. Piani, and L. Tagliacozzo, Simulating the out-of-equilibrium dynamics of local observables by trading entanglement for mixture, *Phys. Rev. B* **99**, 235115 (2019).
- [7] M. Frías-Pérez, L. Tagliacozzo, and M. C. Bañuls, Converting long-range entanglement into mixture: Tensor-network approach to local equilibration, *Phys. Rev. Lett.* **132**, 100402 (2024).
- [8] T. Rakovszky, C. W. von Keyserlingk, and F. Pollmann, Dissipation-assisted operator evolution method for capturing hydrodynamic transport, *Phys. Rev. B* **105**, 075131 (2022).
- [9] C. von Keyserlingk, F. Pollmann, and T. Rakovszky, Operator backflow and the classical simulation of quantum transport, *Phys. Rev. B* **105**, 245101 (2022).
- [10] T. K. Kivorning, L. Herviou, and J. H. Bardarson, Time-evolution of local information: thermalization dynamics of local observables, *SciPost Phys.* **13**, 080 (2022).
- [11] C. Artiago, C. Fleckenstein, D. Aceituno Chávez, T. K. Kivorning, and J. H. Bardarson, Efficient large-scale many-body quantum dynamics via local-information time evolution, *PRX Quantum* **5**, 020352 (2024).
- [12] G. Park, Z. Huang, Y. Zhu, C. Yang, G. K.-L. Chan, and L. Lin, Quasi-lindblad pseudomode theory for open quantum systems, *Phys. Rev. B* **110**, 195148 (2024).
- [13] M. C. Bañuls, M. B. Hastings, F. Verstraete, and J. I. Cirac, Matrix product states for dynamical simulation of infinite chains, *Phys. Rev. Lett.* **102**, 240603 (2009).
- [14] M. B. Hastings and R. Mahajan, Connecting entanglement in time and space: Improving the folding algorithm, *Phys. Rev. A* **91**, 032306 (2015).
- [15] A. Strathearn, P. Kirton, D. Kilda, J. Keeling, and B. W. Lovett, Efficient non-markovian quantum dynamics using time-evolving matrix product operators, *Nature Communications* **9**, 10.1038/s41467-018-05617-3 (2018).
- [16] M. R. Jørgensen and F. A. Pollock, Exploiting the causal tensor network structure of quantum processes to efficiently simulate non-markovian path integrals, *Phys. Rev. Lett.* **123**, 240602 (2019).
- [17] E. Ye and G. K.-L. Chan, Constructing tensor network influence functionals for general quantum dynamics, *The Journal of Chemical Physics* **155**, 10.1063/5.0047260 (2021).
- [18] A. Lerose, M. Sonner, and D. A. Abanin, Influence matrix approach to many-body floquet dynamics, *Phys. Rev. X* **11**, 021040 (2021).
- [19] M. Sonner, A. Lerose, and D. A. Abanin, Influence functional of many-body systems: Temporal entanglement and matrix-product state representation, *Annals of Physics* **435**, 168677 (2021), special issue on Philip W. Anderson.
- [20] M. Frías-Pérez and M. C. Bañuls, Light cone tensor network and time evolution, *Phys. Rev. B* **106**, 115117 (2022).
- [21] A. Foligno, T. Zhou, and B. Bertini, Temporal entanglement in chaotic quantum circuits, *Phys. Rev. X* **13**, 041008 (2023).
- [22] M. Cygorek, M. Cosacchi, A. Vagov, V. M. Axt, B. W. Lovett, J. Keeling, and E. M. Gauger, Simulation of open quantum systems by automated compression of arbitrary environments, *Nature Physics* **18**, 662 (2022).
- [23] N. Ng, G. Park, A. J. Millis, G. K.-L. Chan, and D. R. Reichman, Real-time evolution of anderson impurity models via tensor network influence functionals, *Phys. Rev. B* **107**, 125103 (2023).
- [24] G. Park, N. Ng, D. R. Reichman, and G. K.-L. Chan, Tensor network influence functionals in the continuous-time limit: Connections to quantum embedding, bath discretization, and higher-order time propagation, *Phys. Rev. B* **110**, 045104 (2024).
- [25] J. Thoenniss, M. Sonner, A. Lerose, and D. A. Abanin, Efficient method for quantum impurity problems out of equilibrium, *Phys. Rev. B* **107**, L201115 (2023).
- [26] R. Chen, X. Xu, and C. Guo, Grassmann time-evolving matrix product operators for quantum impurity models, *Phys. Rev. B* **109**, 045140 (2024).
- [27] H. Nguyen, N. Ng, L. P. Lindoy, G. Park, A. J. Millis, G. Kin-Lic Chan, and D. R. Reichman, Correlation functions from tensor network influence functionals: The case of the spin-boson model, *The Journal of Chemical Physics* **161**, 104111 (2024).
- [28] G. E. Fux, P. Fowler-Wright, J. Beckles, E. P. Butler, P. R. Eastham, D. Gribben, J. Keeling, D. Kilda, P. Kirton, E. D. C. Lawrence, B. W. Lovett, E. O'Neill, A. Strathearn, and R. de Wit, Oqupy: A python package to efficiently simulate non-markovian open quantum systems with process tensors, *The Journal of Chemical Physics* **161**, 124108 (2024).
- [29] R. P. Feynman and F. L. Vernon, The theory of a general quantum system interacting with a linear dissipative system, *Annals of Physics* **24**, 118 (1963).
- [30] J. S. Yedidia, W. T. Freeman, and Y. Weiss, Generalized belief propagation, in *Advances in Neural Information Processing Systems*, Vol. 13, edited by T. Leen, T. Dietterich, and V. Tresp (MIT Press, 2000).
- [31] J. S. Yedidia, W. T. Freeman, and Y. Weiss, Understanding belief propagation and its generalizations, in *Explor-*

- ing Artificial Intelligence in the New Millennium* (Morgan Kaufmann Publishers Inc., San Francisco, CA, USA, 2003) pp. 239–269.
- [32] M. Mézard and A. Montanari, *Information, Physics, and Computation* (Oxford University Press, 2009).
- [33] R. Alkabetz and I. Arad, Tensor networks contraction and the belief propagation algorithm, *Phys. Rev. Res.* **3**, 023073 (2021).
- [34] S. Sahu and B. Swingle, Efficient tensor network simulation of quantum many-body physics on sparse graphs (2022), arXiv:2206.04701 [quant-ph].
- [35] N. Pancotti and J. Gray, One-step replica symmetry breaking in the language of tensor networks (2023), arXiv:2306.15004 [quant-ph].
- [36] J. Tindall and M. Fishman, Gauging tensor networks with belief propagation, *SciPost Phys.* **15**, 222 (2023).
- [37] C. Guo, D. Poletti, and I. Arad, Block belief propagation algorithm for two-dimensional tensor networks, *Phys. Rev. B* **108**, 125111 (2023).
- [38] T. Begušić, J. Gray, and G. K.-L. Chan, Fast and converged classical simulations of evidence for the utility of quantum computing before fault tolerance, *Science Advances* **10**, eadk4321 (2024).
- [39] J. Tindall, A. Mello, M. Fishman, M. Stoudenmire, and D. Sels, Dynamics of disordered quantum systems with two- and three-dimensional tensor networks (2025), arXiv:2503.05693 [quant-ph].
- [40] Y. Kim, A. Eddins, S. Anand, K. X. Wei, E. van den Berg, S. Rosenblatt, H. Nayfeh, Y. Wu, M. Zaletel, K. Temme, and A. Kandala, Evidence for the utility of quantum computing before fault tolerance, *Nature* **618**, 500 (2023).
- [41] J. Tindall, M. Fishman, E. M. Stoudenmire, and D. Sels, Efficient tensor network simulation of ibm’s eagle kicked ising experiment, *PRX Quantum* **5**, 010308 (2024).
- [42] H.-J. Liao, K. Wang, Z.-S. Zhou, P. Zhang, and T. Xiang, Simulation of ibm’s kicked ising experiment with projected entangled pair operator (2023), arXiv:2308.03082 [quant-ph].
- [43] S. Patra, S. S. Jahromi, S. Singh, and R. Orús, Efficient tensor network simulation of ibm’s largest quantum processors, *Phys. Rev. Res.* **6**, 013326 (2024).
- [44] A. Lazarides, A. Das, and R. Moessner, Equilibrium states of generic quantum systems subject to periodic driving, *Phys. Rev. E* **90**, 012110 (2014).
- [45] L. D’Alessio and M. Rigol, Long-time behavior of isolated periodically driven interacting lattice systems, *Phys. Rev. X* **4**, 041048 (2014).
- [46] P. Ponte, A. Chandran, Z. Papić, and D. A. Abanin, Periodically driven ergodic and many-body localized quantum systems, *Annals of Physics* **353**, 196 (2015).
- [47] T. Begušić and G. K.-L. Chan, Real-time operator evolution in two and three dimensions via sparse pauli dynamics, *PRX Quantum* **6**, 020302 (2025).
- [48] A. Sinibaldi, D. Hendry, F. Vicentini, and G. Carleo, Time-dependent neural galerkin method for quantum dynamics (2024), arXiv:2412.11778 [quant-ph].
- [49] B. Pirvu, V. Murg, J. I. Cirac, and F. Verstraete, Matrix product operator representations, *New Journal of Physics* **12**, 025012 (2010).
- [50] F. Verstraete and J. I. Cirac, Renormalization algorithms for quantum-many body systems in two and higher dimensions (2004), arXiv:cond-mat/0407066 [cond-mat.str-el].
- [51] F. Verstraete, V. Murg, and J. Cirac, Matrix product states, projected entangled pair states, and variational renormalization group methods for quantum spin systems, *Advances in Physics* **57**, 143 (2008).
- [52] M. Lubasch, J. I. Cirac, and M.-C. Bañuls, Algorithms for finite projected entangled pair states, *Phys. Rev. B* **90**, 064425 (2014).
- [53] M. Lubasch, J. I. Cirac, and M. C. Bañuls, Unifying projected entangled pair state contractions, *New Journal of Physics* **16**, 033014 (2014).
- [54] More precisely, \mathcal{I} reweights the path integral over bond degrees of freedom in Fig. 1b, not over the system degrees of freedom. This object is defined as a boundary influence functional in [24]. In this work, we do not distinguish between the two.
- [55] H. A. Bethe and W. L. Bragg, Statistical theory of superlattices, *Proceedings of the Royal Society of London. Series A - Mathematical and Physical Sciences* **150**, 552 (1935).
- [56] There exists an extension of BP to approximate messages using MPS [37, 39]. However, there is a difference in the way the tensors are grouped. For example, in [37], the main goal is to compute the contraction of a 2D tensor network. Spatial sites are grouped into blocks, and the messages around the blocks are approximated as MPS. In contrast, the main goal of our work is to contract $n + 1$ -dimensional tensor networks (where n is the spatial dimension) in the context of quantum dynamics. A group of tensors is formed around a single site (or cluster of sites), but the message along the time direction is approximated as the MPS.
- [57] A. Lerose, M. Sonner, and D. A. Abanin, Overcoming the entanglement barrier in quantum many-body dynamics via space-time duality, *Phys. Rev. B* **107**, L060305 (2023).
- [58] E. M. Stoudenmire and S. R. White, Minimally entangled typical thermal state algorithms, *New Journal of Physics* **12**, 055026 (2010).
- [59] S. Paeckel, T. Köhler, A. Swoboda, S. R. Manmana, U. Schollwöck, and C. Hubig, Time-evolution methods for matrix-product states, *Annals of Physics* **411**, 167998 (2019).
- [60] M. Akila, D. Waltner, B. Gutkin, and T. Guhr, Particle-time duality in the kicked ising spin chain, *Journal of Physics A: Mathematical and Theoretical* **49**, 375101 (2016).
- [61] B. Bertini, P. Kos, and T. Prosen, Exact correlation functions for dual-unitary lattice models in 1 + 1 dimensions, *Phys. Rev. Lett.* **123**, 210601 (2019).
- [62] C. Jonay, V. Khemani, and M. Ippoliti, Triunitary quantum circuits, *Phys. Rev. Res.* **3**, 043046 (2021).
- [63] S. Anand, K. Temme, A. Kandala, and M. Zaletel, Classical benchmarking of zero noise extrapolation beyond the exactly-verifiable regime (2023), arXiv:2306.17839 [quant-ph].
- [64] K. Kechedzhi, S. Isakov, S. Mandrá, B. Villalonga, X. Mi, S. Boixo, and V. Smelyanskiy, Effective quantum volume, fidelity and computational cost of noisy quantum processing experiments, *Future Generation Computer Systems* **153**, 10.1016/j.future.2023.12.002 (2024).
- [65] Y. Shao, F. Wei, S. Cheng, and Z. Liu, Simulating noisy variational quantum algorithms: A polynomial approach, *Phys. Rev. Lett.* **133**, 120603 (2024).

- [66] M. S. Rudolph, E. Fontana, Z. Holmes, and L. Cincio, Classical surrogate simulation of quantum systems with lowesa (2023), arXiv:2308.09109 [quant-ph].
- [67] Another possible representation is to absorb the ZZ interaction tensors to the edge site tensors, which has been utilized in [18, 19]. The representation of the interaction tensor can affect the numerical results. In the continuous-time limit, the second representation suffers from zero temporal entanglement entropy [19], whereas the SVD-based representation does not [24]. When $|\theta_J| = \pi/2$, the singular value spectrum is uniform, and both schemes yield the same result. When $|\theta_J| \neq \pi/2$, both representations will have the same result in the limit of the infinite bond dimension but have different numerical results in the finite bond dimension.
- [68] We followed the light cone tensor network scheme on the 1D system for the initial guess.
- [69] Ref. [21] analyzes the Schmidt value spectrum of the IF-MPS obtained from 1D lattice dynamics. The Schmidt value spectrum comprises a few slowly decaying large Schmidt values and a long exponential tail of Schmidt values. The TEE from this Schmidt value spectrum is often larger than the EE from a purely exponentially decaying spectrum of Schmidt values.
- [70] A. Lerose, M. Sonner, and D. A. Abanin, Scaling of temporal entanglement in proximity to integrability, *Phys. Rev. B* **104**, 035137 (2021).
- [71] G. Giudice, G. Giudici, M. Sonner, J. Thoenniss, A. Lerose, D. A. Abanin, and L. Piroli, Temporal entanglement, quasiparticles, and the role of interactions, *Phys. Rev. Lett.* **128**, 220401 (2022).
- [72] J. Thoenniss, A. Lerose, and D. A. Abanin, Nonequilibrium quantum impurity problems via matrix-product states in the temporal domain, *Phys. Rev. B* **107**, 195101 (2023).
- [73] R. Kikuchi, A theory of cooperative phenomena, *Phys. Rev.* **81**, 988 (1951).
- [74] M. Chertkov and V. Y. Chernyak, Loop calculus in statistical physics and information science, *Phys. Rev. E* **73**, 065102 (2006).
- [75] A. Montanari and T. Rizzo, How to compute loop corrections to the bethe approximation, *Journal of Statistical Mechanics: Theory and Experiment* **2005**, P10011 (2005).
- [76] A. Pelizzola, Cluster variation method in statistical physics and probabilistic graphical models, *Journal of Physics A: Mathematical and General* **38**, R309 (2005).
- [77] G. Parisi and F. Slanina, Loop expansion around the bethe-peierls approximation for lattice models, *Journal of Statistical Mechanics: Theory and Experiment* **2006**, L02003 (2006).
- [78] H. Zhou and C. Wang, Region graph partition function expansion and approximate free energy landscapes: Theory and some numerical results, *Journal of Statistical Physics* **148**, 513 (2012).
- [79] G. T. Cantwell and M. E. J. Newman, Message passing on networks with loops, *Proceedings of the National Academy of Sciences* **116**, 23398 (2019).
- [80] A. Kirkley, G. T. Cantwell, and M. E. J. Newman, Belief propagation for networks with loops, *Science Advances* **7**, eabf1211 (2021).
- [81] Y. Wang, Y. E. Zhang, F. Pan, and P. Zhang, Tensor network message passing, *Phys. Rev. Lett.* **132**, 117401 (2024).
- [82] G. Evenbly, N. Pancotti, A. Milsted, J. Gray, and G. K.-L. Chan, Loop series expansions for tensor networks (2024), arXiv:2409.03108 [quant-ph].
- [83] P. C. G. Vlaar and P. Corboz, Simulation of three-dimensional quantum systems with projected entangled-pair states, *Phys. Rev. B* **103**, 205137 (2021).
- [84] Y. Gao, H. Zhai, J. Gray, R. Peng, G. Park, W.-Y. Liu, E. F. Kjønstad, and G. K.-L. Chan, Fermionic tensor network contraction for arbitrary geometries (2024), arXiv:2410.02215 [quant-ph].
- [85] B. Tang, E. Khatami, and M. Rigol, A short introduction to numerical linked-cluster expansions, *Computer Physics Communications* **184**, 557 (2013).
- [86] H. C. Jiang, Z. Y. Weng, and T. Xiang, Accurate determination of tensor network state of quantum lattice models in two dimensions, *Phys. Rev. Lett.* **101**, 090603 (2008).
- [87] S. S. Jahromi and R. Orús, Universal tensor-network algorithm for any infinite lattice, *Physical Review B* **99**, 195105 (2019).
- [88] P. Czarnik, J. Dziarmaga, and P. Corboz, Time evolution of an infinite projected entangled pair state: An efficient algorithm, *Phys. Rev. B* **99**, 035115 (2019).
- [89] J. Dziarmaga, Time evolution of an infinite projected entangled pair state: Neighborhood tensor update, *Phys. Rev. B* **104**, 094411 (2021).
- [90] J. Dziarmaga, Time evolution of an infinite projected entangled pair state: A gradient tensor update in the tangent space, *Phys. Rev. B* **106**, 014304 (2022).
- [91] M. Schmitt and M. Heyl, Quantum many-body dynamics in two dimensions with artificial neural networks, *Phys. Rev. Lett.* **125**, 100503 (2020).
- [92] H. W. J. Blöte and Y. Deng, Cluster monte carlo simulation of the transverse ising model, *Phys. Rev. E* **66**, 066110 (2002).
- [93] A. Sinibaldi, D. Hendry, F. Vicentini, and G. Carleo, Private communications.
- [94] A. D. King, A. Nocera, M. M. Rams, J. Dziarmaga, R. Wiersema, W. Bernoudy, J. Raymond, N. Kaushal, N. Heinsdorf, R. Harris, K. Boothby, F. Altomare, M. Asad, A. J. Berkley, M. Boschnak, K. Chern, H. Christiani, S. Cibere, J. Connor, M. H. Dehn, R. Deshpande, S. Ejtemaee, P. Farre, K. Hamer, E. Hoskinson, S. Huang, M. W. Johnson, S. Kortas, E. Ladizinsky, T. Lanting, T. Lai, R. Li, A. J. R. MacDonald, G. Marsden, C. C. McGeoch, R. Molavi, T. Oh, R. Neufeld, M. Norouzpour, J. Pasvolsky, P. Poitras, G. Poulin-Lamarre, T. Prescott, M. Reis, C. Rich, M. Samani, B. Sheldan, A. Smirnov, E. Sterpka, B. T. Clavera, N. Tsai, M. Volkmann, A. M. Whitar, J. D. Whittaker, W. Wilkinson, J. Yao, T. Yi, A. W. Sandvik, G. Alvarez, R. G. Melko, J. Carrasquilla, M. Franz, and M. H. Amin, Beyond-classical computation in quantum simulation, *Science* **0**, ead6285 (2025).
- [95] R. Haghshenas, E. Chertkov, M. Mills, W. Kadow, S.-H. Lin, Y.-H. Chen, C. Cade, I. Niesen, T. Begušić, M. S. Rudolph, C. Cirstoiu, K. Hemery, C. M. Keever, M. Lubasch, E. Granet, C. H. Baldwin, J. P. Bartolotta, M. Bohn, J. Cline, M. DeCross, J. M. Dreiling, C. Foltz, D. Francois, J. P. Gaebler, C. N. Gilbreth, J. Gray, D. Gresh, A. Hall, A. Hankin, A. Hansen, N. Hewitt, R. B. Hutson, N. Kotibhaskar, E. Lehman, D. Lucchetti, I. S. Madjarov, K. Mayer, A. R. Milne, B. Neyenhuis, G. Park, B. Ponsioen, P. E. Siegfried, D. T. Stephen,

B. G. Tiemann, M. D. Urmey, J. Walker, A. C. Potter, D. Hayes, G. K.-L. Chan, F. Pollmann, M. Knap, H. Dreyer, and M. Foss-Feig, Digital quantum magnetism at the frontier of classical simulations (2025),

arXiv:2503.20870 [quant-ph].
[96] J. Gray, quimb: A python package for quantum information and many-body calculations, *Journal of Open Source Software* **3**, 819 (2018).